Journal of Field Robotics

WILEY

RESEARCH ARTICLE OPEN ACCESS

Evaluation of Two Tension Sensors for Cable-Driven Parallel Manipulators

Angel G. Gonzalez-Rodriguez[1] | Erika Ottaviano[2] | Pierluigi Rea[3]

[1]Department of Electronic Engineering and Automation, University of Jaen, Jaen, Spain | [2]Department of Civil and Mechanical Engineering, University of Cassino and Southern Lazio, Cassino, Italy | [3]Department of Mechanical, Chemical and Material Engineering, University of Cagliari, Cagliari, Italy

Correspondence: Angel G. Gonzalez-Rodriguez (agaspar@ujaen.es)

Received: 3 May 2024 | **Revised:** 3 August 2024 | **Accepted:** 9 September 2024

Funding: This research was supported by the University of Jaen.

Keywords: actuator dynamics | cable-driven parallel manipulators | supervisory control | tension sensor

ABSTRACT

Cable-driven parallel manipulators (CDPMs) constitute a class of parallel robots in which the frame is connected to the end-effector through a set of cables. The weight reduction achieved by replacing rigid links with cables, along with their exceptionally large workspace, makes CDPMs suitable for applications such as positioning devices, large surface inspection, motion support systems, and automated storage systems. For effective use in these applications, accurate positioning capabilities are essential, which in turn require accurate measurements of the tension on each cable, and at a sampling rate that is less than or equal to the time constant of the actuator response. This paper first analyses the dynamics of the actuator for an over-constrained robot and provides concrete values of this constant considering the cable elasticity. Then, it proposes two tension sensors, presents the calibration procedures, and the methodologies to evaluate them in CDPMs so that they can be replicated and subsequently included in another CDPM configuration. They also serve as critical safety devices, continuously monitoring cable tension to detect any operations or situations that are out of range. Ensuring the safe and reliable condition of cables is crucial not only for CDPMs but also for lifting systems, transmission systems, and other mechanical or mechatronic systems that rely on cables.

1 | Introduction

In cable-driven parallel manipulators (CDPM) the position and orientation of the end-effector (EE) can be controlled by adjusting the lengths of a set of cables (Merlet 2000). Replacing rigid link by cables offers several advantages. Firstly, the flexibility of cables allows for easy rolling and unrolling, enabling much longer actuator strokes in cable robots compared to traditional parallel machines with rigid links. Despite being flexible, cables have a high tensile capacity. As a result, using cables instead of conventional links and actuators significantly reduces the moving masses, improving both kinematic and dynamic performance. Furthermore, the flexibility of cables allows for easy attachment to the moving platform and helps to mitigate issues related to interference or restricted joint motion.

One of the first CDPMs, the RoboCrane with six degrees of freedom (DoF), was developed by the National Institute of Standards and Technology (NIST) and described in Albus, Bostelman, and Dagalakis (1992). Since then, various applications have emerged, such as the SkyCam (Brown 1985), used as a camera positioning system in sports events, a search and rescue system (Merlet 2008), an industrial pick and place

Abbreviations: BLE, bluetooth low energy; CDPM, cable-driven parallel manipulator; DoF, degree of freedom; EE, end-effector; HSS, high speed shaft; LPF, low pass filter; LSS, low speed shaft.

system (Barbazza et al. 2017), and large-scale 3D printers (Izard et al. 2017; Bosscher et al. 2007).

CDPMs are also utilized in laser distance-measuring devices (Idà, Marian, and Carricato 2020), large-scale solar panel assembly (Pott, Meyer, and Verl 2010), maintenance of vertical green gardens (Schröder 2021), plant monitoring (Chen et al. 2023), and various maintenance or assembly operations involving large surfaces such as airplanes, windows, walls, curtain walls, and facade panels (Iturralde and Bock 2018). Current studies keep revealing new potential uses for CDPM.

Despite the growing number of applications, several challenging issues need to be addressed for the proper use of CDPMs. One key factor is obtaining proper and confident measurements of their cable tensions, which are essential for the precise positioning of CDPMs in applications such as large surface inspections or manipulation, large-scale 3D printing, and automated storage systems. For example, in the case of manipulating heavy objects in large workspaces, significant positioning errors may appear. These errors can be alleviated by introducing the measurement of cable tension into the positioning control algorithm. Additionally, the measurement of cable tensions can be extended to any mechanical or mechatronic systems using cables such as: lifting systems, to detect overload or unreliable operation; power transmission systems, to ensure an adequate tension in the transmission chain; tension legs in floating offshore wind turbines, to guarantee an adequate level of tension in the tendons that anchor the platform to the seabed, keeping the platform stable; and in general, as critical safety device, detecting anomalies and out-of-range occurrences for any device actuated by means of cables, by continuously monitoring the tension during cable operation, thereby ensuring the secure use of the system.

Traditionally, the reference for the tensions of cables is obtained from the external forces and torques, using the wrench matrix, and ensuring all tension components are positive since cables can only pull (Roberts, Graham, and Lippitt 1998). This leads to the Wrench-Feasible Workspace (WFW), as the set of poses where the EE is fully controllable (Bosscher, Riechel, and Ebert-Uphoff 2006). To optimize cable tension distribution, methods like Linear Programming, Quadratic Programming, and the Closed-Form Method are used. High-speed control scenarios require cable tensions close to the average within limits to avoid motor overload and maintain stiffness. This study employs the Closed-Form Method (Pott, Bruckmann, and Mikelsons 2009) for optimal tension distribution. Additionally, Yang et al. (2022) use an adaptive extended Kalman filter to identify the cable forces, which is advantageous for real-time control due to its fast computation time.

Beyond these cable tension estimations, some works are also found with experimental setups for the tension measurement. In Ottaviano, Ceccarelli, and Palmucci (2009), tension sensors are integrated into a cable-based parallel manipulator to experimentally identify human walking characteristics. Kraus, Kessler, and Pott (2015) list different types of tension sensors and analyze the impact of friction on CDPM control. Rubio-Gómez et al. (2021) introduce a novel system with three pulleys for installation in CDPMs, and Thanh and Truong Thinh (2022) present an experimental setup for measuring cable tension in a planar 4-CDPM.

Following this line of new experimental setups for measuring cable tensions, in this paper, two new setups are proposed that can be included in a CDPM. The first type of tension sensor must be placed in series with the cable, close to the EE. The second type consists in a load-cell attached to a small pulley pushed by the cable, where the force exerted over the loadcell is proportional to the cable tension. It must be positioned between two pulleys guiding the cable, or between a pulley and the drum.

This paper proposes effective solutions for experimental apparatus used in cable tension evaluations that are general and applicable to all designs, barely requiring mechanical modifications to existing systems. Based on this aim, the main contributions of this article are as follows:

- The dynamics of the actuator block of a winch in a CDPM have been modelled, obtaining its time constant. The effect of the cable elasticity of multi-stranded steel cable is also included.
- Two new measuring setups are proposed and described to measure the cable tension in a CDPM, explaining their operating principles and their connections to a control unit. They present better performance in terms of applicability, replicability, easy layout or less interference than other prototypes found in the literature.
- The operation, attachment to the CDPM and calibration procedures for both sensors are described, and all the information necessary for its replication is available.
- The discrepancy between the tension values estimated from the actuator's armature current and those measured by the sensors are visualized. If the armature current of a motor is used to estimate the tension in the cable driven by that motor, significant errors will occur, adversely affecting the EE position accuracy.

The rest of the paper is structured as follows. Section 2 describes the planar 4-CDPM where the sensors were tested, details the governing dynamics equations, and highlights the importance of tension monitoring for improving robot performance. Section 3 examines the electro-mechanical dynamics of the actuator to determine its characteristic time. Section 4 describes the operation and setups, and calibration results for both types of sensors. Section 5 compares the performance of both sensor types against an estimation obtained from the actuator currents. Finally, Section 6 discusses the key features of the proposed sensors and the future lines of improvement.

2 | Planar 4 CDPM. Dynamic Model

A planar version of a CDPM, located at the Laboratory of Robotics and Mechatronics, University of Cassino, Italy, has been used for the evaluation of the tension sensors. It has three DOFs that allow the movement of the EE in the XZ plane and adjust its orientation. The planar setup is shown in Figure 1.

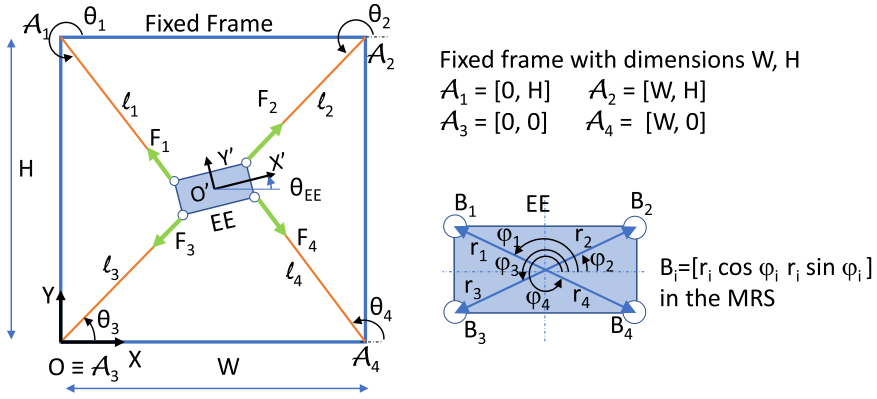

FIGURE 1 | A schematic of the 4 planar CDPM and the main kinetostatic parameters.

The points $\mathcal{A}_j$ at the fixed frame define the positions of the exit points for the four cables ($j = 1 \dots 4$). A stationary reference frame OXY is fixed at point $\mathcal{A}_3$, and a moving reference system (MRS) O'X'Y' is located at the EE center P_{EE}, rotated by a certain angle θ_{EE}. B_j is the position, referred to the MRS, of point where cable j is attached to the EE, described as $r_j e^{\mathbf{i}\varphi_j}$ in the MRS, as shown in Figure 1. Actuators adjust the length of the cables from the attachment points to the EE by winding and unwinding them around drums. These cable lengths ℓ_j ($j = 1 \dots 4$) can be determined by:

$$\ell_j = \|\mathcal{A}_j - (P_{EE} + RB_j)\| \quad \text{with} R = \begin{bmatrix} \cos(\theta_{EE}) & -\sin(\theta_{EE}) \\ \sin(\theta_{EE}) & +\cos(\theta_{EE}) \end{bmatrix} \tag{1}$$

or also

$$\ell_j = \|A_j - \left(P_{EE} + r_j e^{\mathbf{i}(\theta_{EE}+\varphi_j)}\right)\|. \tag{2}$$

In its simplest format, each new desired length for each cable ℓ_j is achieved by moving each winch a number of radians $\Delta\alpha_j$ equal to the increment in cable length $\Delta\ell_j$ divided by the radius of the drum r

$$\Delta\alpha_j = \frac{\Delta\ell_j}{r}. \tag{3}$$

Assuming that $\mathbf{F^e}$ and $\mathbf{M^e}$ are respectively the resultant force and torque exerted on the EE, for a CDPM configuration that belongs to the WFW, the equilibrium of forces and torques with respect to the cable tensions τ_j yields

$$\begin{aligned} F_x^e &= \sum_{j=1}^{4} \tau_j \cos(\theta_j) \\ F_y^e &= \sum_{j=1}^{4} \tau_j \sin(\theta_j) \\ M^e &= \sum_{j=1}^{4} \tau_j \times e^{\mathbf{i}(\theta_{EE}+\varphi_j)} B_j = \overrightarrow{u_z} \sum_{j=1}^{4} \tau_j r_j \sin(\theta_{EE} + \varphi_j - \theta_j) \end{aligned} \tag{4}$$

with τ_j positive working in tension. This equilibrium of forces and torques can be written through the *Structure Matrix A*

$$A\boldsymbol{\tau} = \mathbf{W} \quad \text{with } \mathbf{W} = \left[F_x^e \; F_y^e \; M^e\right]^T. \tag{5}$$

Indeed, for the static equilibrium, and assuming a mass m_{EE} for the EE, it holds

$$\mathbf{W} = [0 \; -m_{EE}\, g \; 0]^T. \tag{6}$$

Similar expressions can be deduced for non-static operations by including the corresponding terms for friction and inertia.

A feasible force distribution must fulfil (5) and (6), ensuring that all tensions remains between $\tau_{\min}$, which is the minimum force in the cables to keep them tensioned, and $\tau_{\max}$, which is the maximum value due to actuator torque limitations that prevent exceeding the cable's breaking load

$$A\boldsymbol{\tau} = \mathbf{W} \quad \text{s.t. } 0 \le \tau_{\min} \le \tau_j \le \tau_{\max} \quad \forall\, \tau_j \in \boldsymbol{\tau}. \tag{7}$$

For underdetermined systems, with more unknowns (the cable tensions) than equations, there are infinity of possible solutions as noted in Bruckmann et al. (2008). From them, the one with the lowest energetic value τ_{lev} is the one obtained with the Moore-Penrose inverse A^+:

$$\boldsymbol{\tau}_{lev} = A^+\mathbf{W} \quad \text{with} \quad A^+ = A^T(AA^T)^{-1} \tag{8}$$

that provides the solution with the minimum Euclidean norm. However, rather than searching for the lowest energetic value, it is essential to ensure that the solution adheres to the tension limits. Identifying a feasible tension distribution presents a challenge in terms of both design and control.

To this end, expressions (1) to (8) theoretically link the rotations imposed by the actuators and the cable tensions, once known the external and dynamical forces and torques.

However, there are phenomena that give rise to inaccuracies in the positioning of the EE such as sagging, cable elasticity, slack in the winch, and so forth. Most of these inaccuracies can be alleviated by measuring the tensions in the cables. Figure 2 shows the block diagram for the trajectory control that includes the tension measurements for a more accurate evaluation of the cable lengths (Piao et al. 2019). This is especially important in the case of

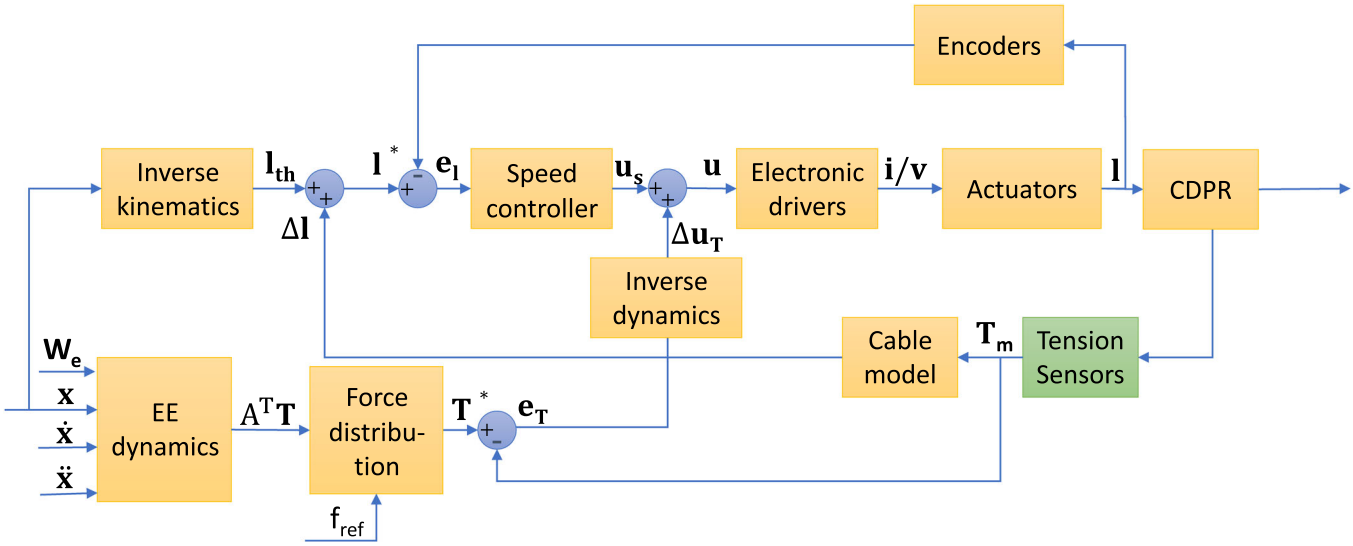

FIGURE 2 | Block diagram for the trajectory control of the EE combining tension measurement for a more accurate evaluation of the cable lengths.

manipulating heavy objects, where the presence or absence of the transported object along a large workspace can lead to significant inaccuracies in positioning. Feedback of the cable tensions allows the control loop to modify the angle references commanded to the actuator to properly account for these deviations.

The inner control time step is typically in the order of 1 ms (Kraus, Kessler, and Pott 2015; Thanh and Truong Thinh 2022). However, the transient in the variation of the cable length, and consequently, that of their tensions exhibits slower dynamics. By analyzing the electro-mechanical dynamics, in the following section, it will be shown that it is around 80 ~ 100 ms for the actuators used in this work. This time allows the designer to establish a value of time below which is necessary to acquire the cable tensions.

The cable tension measurement is also valuable to avoid an excessively high or low value in the cable tensions, while ensuring that the distribution of tensions compensates for the external forces exerted by the winch set. A very high tension value overloads the motors, increases their consumption, causes fatigue problems, and in an extreme case can cause breakage in some of the components. A very low value causes slackening, inadequate winding of the cable on the drum or even the cable coming out of the pulley.

A more simplified scheme like that of Figure 3 is preferred when the accuracy requirements are relaxed but a tension monitoring is still required to keep the cable tension within minimum and maximum limits.

In the case of using tension sensors as supervisory devices, a response time as low as possible is required to avoid problems derived from a robot malfunction.

3 | Electro-Mechanical Dynamic Model of the Actuators

This section describes the controller unit, the electrical dynamics of the motor rotor, and the mechanical dynamics of the chain from the rotor to the drum. Once obtained, the characteristic time of the system composed of the winch will be deduced, to establish a lower limit of the time below which it does not make sense to capture the measurement of the cable tension. These components are represented in Figure 3.

3.1 | Description of the Controller and Actuators

The cable lengths are modified by the set of actuator/drum shown in Figure 4. The drum is allowed to displace longitudinally so that it advances (to the right) as long as the cable is being rolled in. If the cable width and the thread pitch match, then the cable is evenly rolled in, and the exit point of the cable remains invariant when the drum rotates.

The motors used are brushed DC motors, 24 V, 150 W (Maxon RE40, ref 148867), with an attached gearbox (ref 203119). Their parameters are given in Table 1. The rated values, electrical and mechanical, are given in Table 2.

The parameters of the attached gearbox and the remaining mechanical parameters are listed in Table 3. The procedures to obtain the friction parameter and the coefficient of elasticity are detailed in Appendices A and B.

The position feedback is accomplished with an incremental encoder also attached to the motor, with 256 pulses per turn (1024 quads per turn).

In the following, B and J refer to the coefficients for the dynamic friction and inertia, respectively. The superscripts *HSS* (high-speed shaft) and *LSS* (low-speed shaft) refer to the internal shaft of the motor and its external shaft, respectively, the latter being attached to the drum.

$$B_{rotor}^{HSS} = \frac{k_{\phi}^{\tau} I_0}{\omega_0}. \tag{9}$$

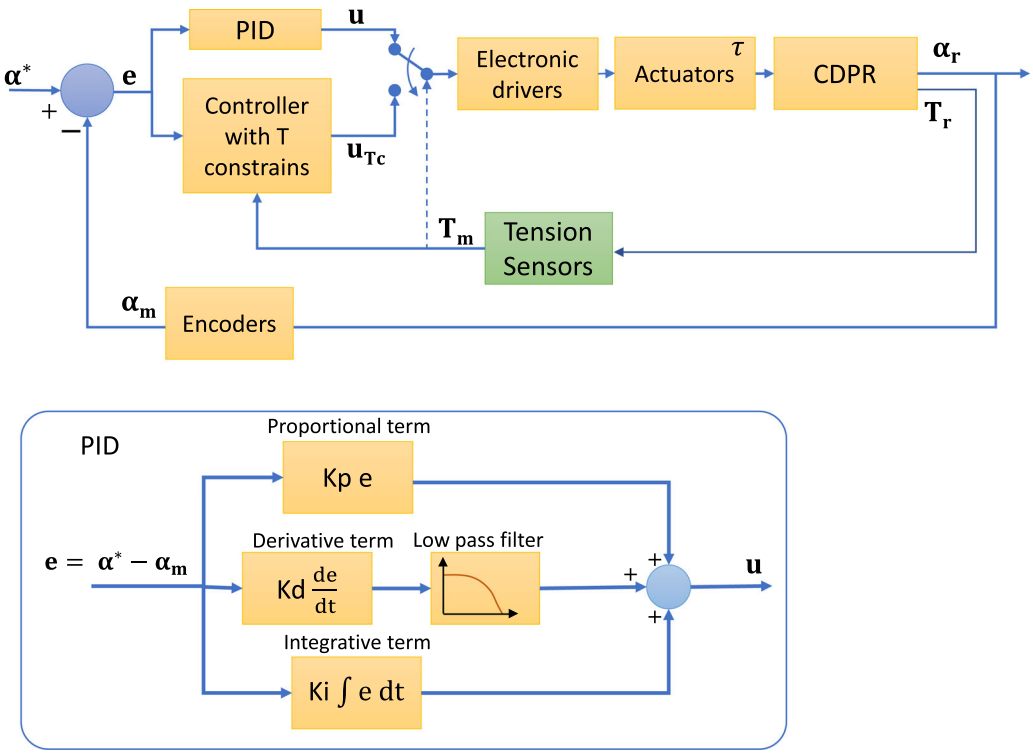

FIGURE 3 | Block diagram for the trajectory control of the EE with supervision of the tension.

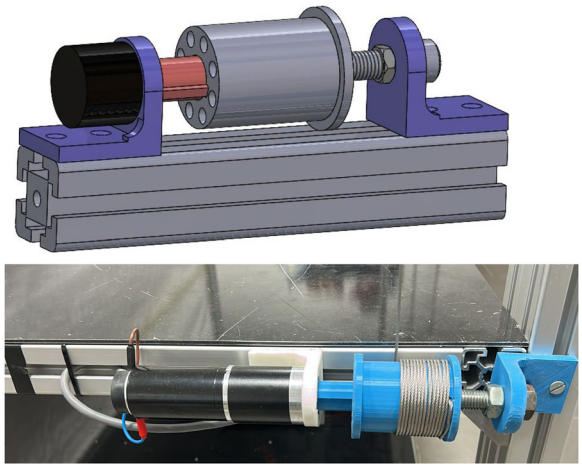

FIGURE 4 | Set of motorreductor and drum for each cable.

Every DC motor is driven by a servoamplifier ESCON 70/10, and the four servoamplifiers are commanded by a single MyRIO 1900, which is a reconfigurable I/O (RIO) device, programmed in LabView (see Figure 5).

3.2 | Modelling Controller, Electronic Drives and Actuator

3.2.1 | Electronic Drivers

To perform a certain trajectory, the reference evolution for all motors as well as the controller structure must be programmed in Labview and transferred to the MyRIO which, at each time step, commands the four servoamplifiers that supply the corresponding motors. To model the driver, the electrical dynamics of the motor armature must be taken into account, as well as the mechanical dynamics of its rotor and gear train. For the electrical dynamics in the Laplace domain, we have

$$U(s) = R_a I_a(s) + L_a I_a s + k_\phi^v \omega_{HSS}(s) \simeq R_a I_a(s) + k_\phi^v \alpha^{LSS}(s) r_{gb} s, \tag{10}$$

where $U(s)$ is the voltage applied to the armature terminals, R_a is the armature resistance, $I_a(s)$ is the armature current, L_a is the armature inductance (which has been neglected as is usually the case in studies of electro-mechanical transients), k_ϕ^v is the speed motor constant linking electromotive force and rotor speed, ω_{HSS} is the speed in the rotor, that is, in the high speed shaft (HSS), α^{LSS} is the rotation angle of the drive axis in the low speed axis (LSS), and r_{gb} is the gearbox ratio. In the following, and for simplicity, the variables and parameters referred to HSS will keep this superscript, but the values referred to LSS will appear without it.

This servoamplifier model includes an internal current control loop, which means that it accepts a current reference as an input that will be followed by the device. Even so, this inner controller behaves according to the dynamics described by (10).

3.2.2 | PID Controller

As for the controller unit, a PID is the preferred option to establish every cable length. To this aim, incremental encoders are usually disposed at the rotor shaft of each motor that provide the

TABLE 1 | Maxon RE40 electrical and mechanical parameters, obtained from the manufacturer.

R_a (Ω)	L_a (mH)	k_ϕ^T (Nm/A)	k_ϕ^v (V/rpm) ($V\ s/rad$)	J_{rotor}^{HSS} (kg m^2)	B_{rotor}^{HSS} (kg m^2/s)
0.299	0.082	0.0302	1/317 *0.0301*	1.42×10^{-5}	5.21×10^{-6}[a]

[a]Obtained from $B_{rotor}^{HSS} = \frac{k_\phi^T I_0}{\omega_0}$.

TABLE 2 | Electrical and mechanical rated values for the Maxon motors.

Rated voltage, U_N	Rated current, I_N	Rated torque at HSS, T_N^{HSS}	Gearbox ratio, r_{gb}	Rated torque at LSS, T_N^{LSS}	No-load	
					Current, I_0	Speed, ω_0
24V	6A	0.177Nm	1:26	4.602Nm	0.137 A	7580 rpm

TABLE 3 | Mechanical parameters for the gearhead and drum.

J_{gb} (kg m^2)	J_{drum} (kg m^2)	Backlash	$B_{gb+drum}$ (kg m^2/s)	τ_{fr}^{st} (kg m^2/s^2)
6.15×10^{-4}	5.04×10^{-5}	0.8 deg	0.035	0.152

FIGURE 5 | Controller unit consisting of MyRIO 1900 and four servoamplifiers ESCON 70/10.

controller with the actual angle increment for each actuator. This actual angle is subtracted from the angle reference, yielding an error $e_\alpha(t)$. The PID controller uses this error to determine the servoamplifier input (in this case the current armature $i_a(t)$). A PID controller can be defined in two different ways:

$$PID_{trad}(s) = \frac{I_a(s)}{E_\alpha(s)} = K_p + K_d \frac{\omega_c}{\omega_c + s} s + Ki \frac{1}{s}, \tag{11}$$

$$PID_{trad}(s) = \frac{I_a(s)}{E_\alpha(s)} = Kp\left(1 + t_d s + \frac{1}{t_i s}\right), \tag{12}$$

where $I_a(s)$ and $E_\alpha(s)$ are the Laplace transforms of $i_a(t)$ and $e_\alpha(t)$; K_p, K_d and K_i are, respectively, the proportional, derivative and integral gains; and t_d and t_i are the derivative time and the integral time, respectively.

A low-pass filter (LPF) has been included to average the excessively changing value for the derivative term. Its transfer function is

$$\begin{aligned} PID_{LPF}(s) &= Kp\left(1 + \frac{\omega_c}{\omega_c + s} t_d s + \frac{1}{t_i s}\right) \\ &= K_p \frac{\left(t_i^2 + t_d t_i \omega_c\right) s^2 + (\omega_c t_i + 1) s + \omega_c}{s(s + \omega_c) t_i}, \end{aligned} \tag{13}$$

where ω_c is the LPF cut-off frequency.

To determine the cut-off frequency, we start from the actual implementation of the filter. It is programmed as

$$u_k^{d,f} = (1 - k_u) u_{k-1}^{d,f} + k_u u_k^d, \tag{14}$$

where k_u is the update constant of the low-pass filter, u_k^d is the derivative term of the controller at instant k, $u_{k-1}^{d,f}$ is its filtered value at the previous time, and $u_k^{d,f}$ is the filtered value calculated at instant k. For a certain sample time (ts), it can also be written as

$$ts \frac{\Delta u_k^{d,f}}{ts} + k_u u_{k-1}^{d,f} = k_u u_k^d. \tag{15}$$

Assuming increments as infinitesimals and moving to the Laplace domain, it yields

$$tsU^{d,f} s + k_u U^{d,f} = k_u U^d \Rightarrow \frac{U^{d,f}}{U^d} = \frac{k_u}{tss + k_u}$$

resulting $\omega_c = k_u / ts$.

Table 4 shows the gain values for the cascade PID controller together with the cut-off frequency of the low-pass filter. It should be pointed out that the high value of the integral gain allows the controller to reduce the tracking error during the motor accelerations and reduce the time to reach the reference.

3.2.3 | Mechanical Dynamics

The mechanical component exhibits nonlinear behavior, which prevents obtaining a generic transfer function for the entire workspace. Instead, increments will be obtained relative to a specific situation, specifically the initial position of a movement.

Moreover, including the cable elasticity in the dynamics of the cable is complex and entails an analysis of the whole CDPM configuration and a study of the tension distribution together with the external forces and the geometrical pose of the end-effector.

This makes it difficult to draw conclusions from analytical results. In an initial approach to determine the time constant of the actuator system, the simplified one-dimensional configuration in Figure 6 (Setup 1) will be studied, which includes an antagonistic actuation to the cable under study. To analyze the effect of motor actuation on the cable tension dynamics, it will be assumed that the antagonistic cable is neither rolled in nor rolled out. In this way, the dynamic effect of the motor actuation on the corresponding cable tension is analyzed in the most unfavorable case (assuming overconstrained CDPM). Setup 1 in Figure 6 shows the simplified model to be analyzed.

Setup 2 corresponds to the most desirable situation (and also the usual one in overconstrained CDPMs), where both actuators move in synchronization. This case is easier to study because the actuator at the right can be suppressed and take into account only one spring whose coefficient of elasticity is the sum of the other two.

TABLE 4 | Gain values for the PID controller and cut-off frequency of the low-pass filter.

Kp	Kd (t_d)	Ki (t_i)	ω_c (rad/s)
6	0.17 (0.0283)	12 (0.500 s)	$k_u/ts = 0.2/0.001$

At the actuator:

If the cable elasticity is disregarded, the mechanical dynamics of the set rotor + gearbox + drum is given by the torque equilibrium

$$k_{\phi}^{\tau} i_a(t) r_{gb} = \tau(t) + \tau_{fr}^{st} + J_t \ddot{\alpha} + B_t \dot{\alpha} \tag{16}$$

with

$$\begin{aligned} \tau(t) &= T(t) r, \\ J_t &= J_{rotor}^{HSS} r_{gb}^2 + J_{gb} + J_{drum}, \\ B_t &= B_{rotor}^{HSS} r_{gb}^2 + B_{gb} + B_{drum}, \end{aligned} \tag{17}$$

where T is the tension at the cable, $\tau(t)$ is the torque at the drum, k_{ϕ}^{τ} is the torque motor constant linking current and torque, τ_{fr}^{st} are the torque losses due to Coulomb or static friction at the gearbox and drum screw, J is the coefficient of inertia and B is the friction coefficient for the components involved (rotor, gearbox, and drum). At the drum, the friction (static and dynamic) is due to the movement between the static screw and the rotating drum nut. For the rotor, the coefficient values are given with respect to the HSS, but can be translated to the LSS by multiplying by r_{gb}^2. These coefficient values for gearbox and drum, as well as torques, are referred to the LSS. With regard to the torque losses due to static friction, its model as

$$\tau_{fr}^{st} = \left|\tau_{fr}^{st}\right| sign(\dot{\alpha}) \tag{18}$$

converts the dynamics into a strongly nonlinear phenomenon, which distances the real dynamics from the expected linear dynamics when a change in the direction of movement of the motors occurs. Although the Dahl model is preferred for a more accurate estimation of the friction, for a first estimation of

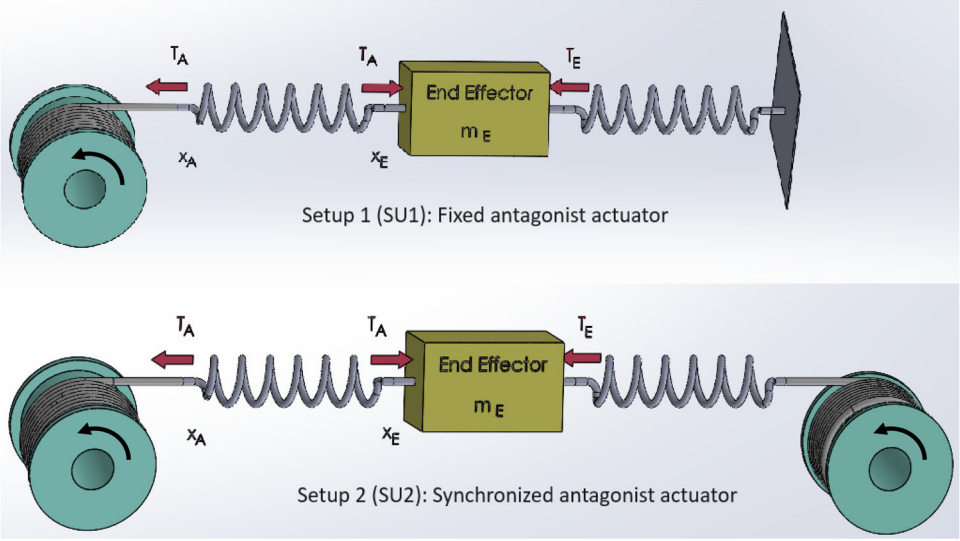

FIGURE 6 | Simplified representations to analyze cable tension dynamics in a one-dimensional configuration in two situations: up, situation with the antagonistic actuator fixed (Setup 1); down, situation with both actuators synchronized (Setup 2).

the characteristic time, the traditional friction model has been used. The gear train backlash also contributes to this non-linearity, although due to its low value (see Table 3), it has not been finally taken into account.

It is worth stating that k_ϕ^v and k_ϕ^τ are theoretically equal. However, additional phenomena such as the armature reaction reduce the electromagnetic flux inside the motor and consequently also the available torque, which for practical purposes is equivalent to a reduction in k_ϕ^τ. In the case of the motor considered, these constants are practically the same, as seen in Table 1.

Including the cable elasticity:

In this case (16) converts into

$$\begin{aligned} k_\phi^\tau i_a(t) r_{gb} - \tau_{fr}^{st} - J_t\ddot{\alpha} - B_t\dot{\alpha} &= T_{A,E} r\ , \\ T_{A,E} + m_E\ddot{x}_E &= T_{B,E}\ , \\ x_A &= -\alpha\ r, \end{aligned} \tag{19}$$

where positive values of $i_a(t)$, α, $T_{A,E}$, and $T_{B,E}$ are considered to be those that result in tension in the cable. The tensions cause stretching in the cables according to

$$\begin{aligned} T_{A,E} &= K_A(x_E - x_A - \epsilon_A), \\ T_{B,E} &= K_B(\epsilon_B - x_E), \end{aligned} \tag{20}$$

where ϵ_B is the position of the EE at which the tension $T_{B,E}$ is zero, and ϵ_A is the extension of the cable when not subjected to tension. Linearization is only possible around a working point, which allows assuming that ϵ_A and ϵ_B are constant. With this, the following variable changes can be made:

$$\delta x_E := x_E - \epsilon_B \tag{21}$$

$$\delta x_A := x_A - \epsilon_A + \epsilon_B \tag{22}$$

yielding

$$T_{A,E} = K_A(\delta x_E - \delta x_A), \tag{23}$$

$$T_{B,E} = -K_B\ \delta x_E. \tag{24}$$

It is also worth mentioning that the value of the elastic coefficient is given by Young's modulus E, the cable cross section S, and the length of the cable from the drum to the EE, given by $\alpha\ r$. Although it is a variable value, by assuming short displacements in relation to the total length of the transmission chain drum-EE, K_A can be considered constant.

To obtain the transfer function (which requires linear behavior), some approximations and variable changes must be made, valid in the vicinity of the initial point of movement:

- With regard to the current, we will take current increments over I_{fr}, which is the value that compensates the static friction τ_{fr}^{st}. This dynamics refers to the quotient between the transient response of the angle at the LSS, and the signal control imposed by the controller unit, once subtracted I_{fr}.
- The values of ϵ_A and ϵ_B that appear in (22) refer to the elongations of the cables to the left and right of the EE, respectively, at which the tensions in those cables are zero. Given the high value of the elasticity constant, the elongation value of each cable, and generally $\epsilon_A - \epsilon_B$, will not vary significantly with respect to the other terms in (19), so in that expression, $-\dot{\alpha}\ r = \dot{x_A} \simeq \delta\dot{x}_A$ holds.

With this, the formulation of the dynamics is as follows, where the transformation to the Laplace domain is also represented:

$$\begin{aligned} T_{A,E}(t) = \frac{k_\phi^\tau \delta i_a(t) r_{gb}}{r} + J_t\frac{\delta\ddot{x}_A}{r^2} + B_t\frac{\delta\dot{x}_A}{r^2} &\Rightarrow T_{A,E}(s) = \frac{k_\phi^\tau I_a r_{gb}}{r} + J_t\frac{X_A s^2}{r^2} + B_t\frac{X_A s}{r^2} \\ T_{A,E}(t) = T_{B,E}(t) - m_E\delta\ddot{x}_E &\Rightarrow T_{A,E}(s) = T_{B,E}(s) - m_E X_E s^2 \\ T_{A,E}(t) = K_A(\delta x_E - \delta x_A) &\Rightarrow T_{A,E}(s) = K_A(X_E - X_A) \\ T_{B,E}(t) = -K_B\delta x_E &\Rightarrow T_{B,E}(s) = -K_B X_E \end{aligned} \tag{25}$$

where $T_{A,E}(s)$, $T_{B,E}(s)$, $I_a(s)$, $X_A(s)$, and $X_E(s)$ are the Laplace transforms of $T_{A,E}(t)$, $T_{B,E}(t)$, $\delta i_a(t)$, $\delta x_A(t)$, and $\delta x_E(t)$, respectively. These equations are represented in the block diagram of Figure 7.

It is worth mentioning that the servoamplifier current controller dynamics has not been included due to reduced value of its time constant in comparison with the other ones.

Logically, the response is determined by the value of each parameter. The following subsections provide the values, either by inspecting the datasheets or through testing. It also depends on the gains of the PID controller, which performs corrective action on the angle α to match the desired value. The root locus visualizes the dynamics and stability of X_A for different values of the proportional gain K_P of the PID controller. The open-loop transfer function G_{ol} shown in Figure 7 is used to plot the root locus and is given by

$$G_{ol}(s) = PID(s)\frac{(K_A + K_B + m_E s^2)k_\phi^\tau r r_{gb}}{K_A K_B r^2 + B_t s(K_A + K_B) + (J_t(K_A + K_B) + K_A m_E r^2)s^2 + B_t m_E s^3 + J_t m_E s^4} \quad (26)$$

with $PID(s)$ given in (12) or (13).

It is important to note that the diagram in Figure 7, obtained from Figure 6, corresponds to the simplified scheme in which the antagonistic actuator does not move, thereby causing the maximum tension T_A. It is easy to obtain a modified scheme where the antagonistic actuator (which would be on the right) moves in synchronization with the actuator on the left, rotating the same angle (with the opposite sign). In this case

$$\text{Synchronized actuation} \Rightarrow \begin{cases} K_A^{synchr} = K_A + K_B, \\ K_B^{synchr} = 0. \end{cases} \quad (27)$$

In both the case of a stationary antagonistic actuator and the synchronized actuator, for controlling the angle α, its measured value must be fed back to close the loop, which allows for the root locus to be obtained. The analysis of the root locus will provide the dynamics as a function of the K_p constant of the PID controller. This will be discussed in Section 3.3; however, it is first necessary to obtain the specific values of each parameter.

3.3 | Determination of the Characteristic Time

Table 5 visualizes the location of poles and zeros describing the dynamics of $\alpha(t)$ (or correspondingly X_A) when supplying a current $i_a(t)$. There are two groups: the left group using (26) for Setup 1 of Figure 6; and the right group with the simplifications of (27) corresponding to Setup 2 of Figure 6. For each group, the first column corresponds to a scheme with the $PID(s)$ without LPF; in the second, an LPF is included; and in the third, with LPF, the modulus of elasticity used is higher, and more similar to that used in ropes of much larger diameter. For the first two columns, the value of E = 48.9 GPa is used according to Appendix B. For the third column E = 100 GPa according to Feyrer (2007).

For each column, the first pair of zeros and poles depends on the cable elasticity. For a certain column, these poles and zeros have very similar values (all around ±555i or ±793i depending on E) and are very far from the other poles and zeros. Therefore, they can be canceled out and will have little effect on the system's dynamics.

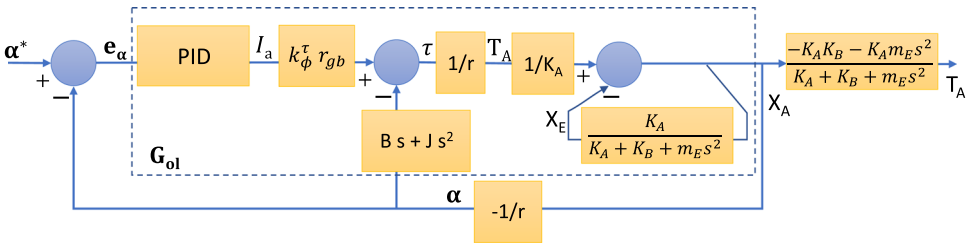

FIGURE 7 | Block diagram for the simplified system including the cable elasticity.

TABLE 5 | Location of zeros and poles describing the dynamics of α for Setup 1 and Setup 2, in three situations: without LPF; with LPF; and with LPF and higher E.

	Setup 1			Setup 2	
$E = 48.9$ GPa without LPF	$E = 48.9$ GPa with LPF	$E = 100$ GPa with LPF	$E = 48.9$ GPa without LPF	$E = 48.9$ GPa with LPF	$E = 100$ GPa with LPF
Zeros	Zeros	Zeros	Zeros	Zeros	Zeros
$0.00 \pm 555.61i$	$-0.00 \pm 555.61i$	$-0.00 \pm 793.73i$	$0.00 \pm 555.61i$	$-0.00 \pm 555.61i$	$-0.00 \pm 793.73i$
$-33.17 + 0.00i$	$-28.17 + 0.00i$	$-28.17 + 0.00i$	$-33.17 + 0.00i$	$-28.17 + 0.00i$	$-28.17 + 0.00i$
$-2.13 + 0.00i$	$-2.13 + 0.00i$	$-2.13 + 0.00i$	$-2.13 + 0.00i$	$-2.13 + 0.00i$	$-2.13 + 0.00i$
Poles	Poles	Poles	Poles	Poles	Poles
$-0.00 \pm 556.03i$	$-0.00 \pm 556.03i$	$-0.00 \pm 794.33i$	$-0.0100 \pm 557.30i$	$-0.0100 \pm 557.30i$	$-0.00 \pm 796.14i$
$-1.84 \pm 21.58i$	$-1.84 \pm 21.58i$	$-1.84 \pm 30.89i$	$0.0 + 0.0i$ Double	$0.0 + 0.0i$ Double	$0.0 + 0.0i$ Double
$0.00 + 0.00i$	$0.00 + 0.00i$	$0.00 + 0.00i$	$-3.66 + 0.00i$	$-3.66 + 0.00i$	$-3.66 + 0.00i$
	$-200.00 + 0.00i$	$-200.00 + 0.00i$		$-200.00 + 0.00i$	$-200.00 + 0.00i$

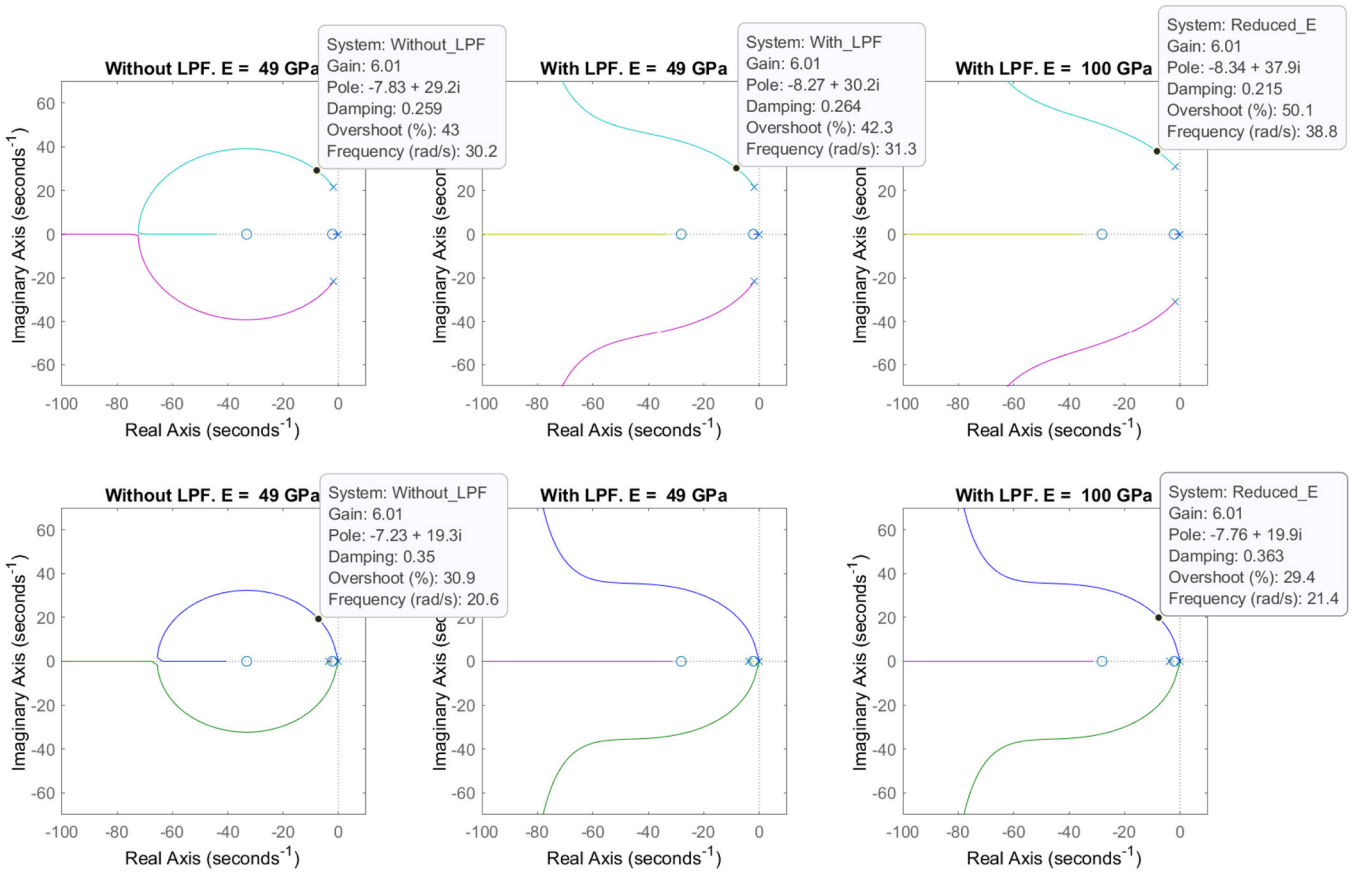

FIGURE 8 | Root locus showing the dynamics of α using a PID with $K_p \simeq 6$. The upper row is for Setup 1 and the lower row for Setup 2. For each row from left to right: without LPF; with LPF; and with LPF and higher E.

For the Setup 1, the second pair of poles is also affected by the value of E and, therefore, by K_A and K_B. After the integrator/s ($s = 0 \pm 0\mathrm{i}$), they are the poles with the lowest modulus, hence being the ones determining the transient response. Their imaginary part significantly increases with E (21.58 for $E = 48.9$ GPa and 30.89 for $E = 100$ GPa), meaning that for stiffer cables:

- the damped natural frequency increases, and the system response is faster,
- a less damped vibration mode is expected.

The pole at $s = 0$ corresponds to the integral term of the PID, and the pole at $s = -200$ is due to the LPF.

For the Setup 2, the cable elasticity has relatively low effect on the position dynamics (the poles determined by K_A are cancelled by very close zeros), and the last two root loci are very similar.

Figure 8 represents the root locus of the actuator dynamics taking into account current increments over I_{fr}, which is the value that compensates the static friction τ_{fr}^{st}. This dynamics refers to the quotient between the transient response of the angle at the LSS, and the signal control imposed by the controller unit, once subtracted I_{fr}. At the central plot, the mentioned LPF has been included (more suitable for real schemes obtaining positions from encoders) and the open-loop transfer function is given by (13) and (26).

$$G_{wLPF}(s) = K_p \frac{\left(t_i^2 + t_d t_i \omega_c\right)s^2 + (\omega_c t_i + 1)s + \omega_c}{s(s + \omega_c)t_i} \frac{\tau_{fr}^{st} r_{gb}}{J_t s^2 + B_t s}. \tag{28}$$

The left-hand plot corresponds to the traditional scheme (more suitable for simulation works) without LPF in the derivative action. Its open-loop transfer function is given by (12) and (26).

$$G_{trad}(s) = K_p \frac{t_d t_i s^2 + t_i s + 1}{t_i s} \frac{\tau_{fr}^{st} r_{gb}}{J_t s^2 + B_t s}. \tag{29}$$

In the setup used for the experiments, the PID controller was tuned with the parameters of Table 4. Hence, the datatip at a gain equal to $Kp = 6$ (6.05 in the plot) represents the transient response of the system. For both configurations, both with and without LPF, the damped natural frequency w_d is highlighted. It is related to the peak time t_p (Ogata 2010) through the expression

$$t_p = \frac{\pi}{w_d}. \tag{30}$$

It can be seen that the damped natural frequency ω_d is around $30\,\mathrm{rad}^{-1}$ when the gain is 6 (the value of Kp in Table 4) and $E = 48.9$ GPa, and around $39\,\mathrm{rad}^{-1}$ for $E = 100$ GPa. This is also true when a low-pass filter is not used. With this value, the peak

time, that can be used as a characteristic time for undamped 2nd-order systems, is in the order of 80 ~ 100 ms. This characteristic time is referred to the drum angle, and consequently to the cable length modification. Since the set of cable lengths determines the cable tensions through the Jacobian matrix, the obtained characteristic time also applies to the evolution of the cable tension. However, the time constant of the tension evolution is not a reliable data to determine how fast a tension sensor should measure in overconstrained CDPM. Indeed, if the antagonist actuator does not move accordingly, a unit change in the position reference can cause a very high-tension value, much higher than that allowed by the system. For example, if a cable gets stuck in the drum or a pulley, or there is a calculation or programming error, the position values will be different to the commanded ones, and may give rise to an unfeasible tension distribution, that will appear with the same characteristic time as the current inner loop controller of the motor (in the order of few ms).

4 | Describing and Calibrating the Sensors

Two new setups for the tension measurement are described in this section, explaining their arrangement in a CDPM, and how they are connected to a microcontroller via amplifier circuits. Each sensor includes a strain gauge that deforms under force, causing a resistance change. This change is amplified by an integrated circuit, which converts it into a digital signal and sends it to the microcontroller through synchronous communication.

4.1 | Description

The three main traditional methods for measuring the cable tensions by means of force sensors are presented in Kraus, Kessler, and Pott (2015) (see Figure 9).

4.1.1 | Inline Force Sensor

This type of sensor directly measures tension and compression forces, by disposing it in series with the cable whose tension is being measured. The proposed inline solution is similar to the first scheme in Figure 9. These solutions do not substantially modify the cable shape, which is especially important if sagging can occur. As disadvantages, both require a radio frequency link for the transmission of measurements and are inadequate for closed-loop configurations such as that of Juárez-Pérez et al. (2021).

However, the inline force sensor allows using reflective pulleys which are a proved way to increase the positioning accuracy as seen in Gonzalez-Rodriguez et al. (2017). Additionally, the in-line arrangement does not hinder the movement of the EE, especially important when the configuration allows a wide range of possible platform orientations as in Carpio Alemán et al. (2019).

Left picture of Figure 10 shows two existing models. Table 6 lists their main characteristics, although these may vary from one manufacturer to another. This work uses a submodel with a measurement range of 0 ~ 10 kg.

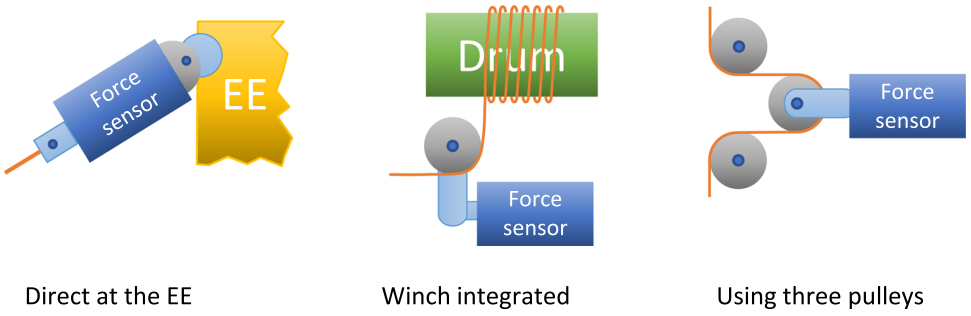

FIGURE 9 | Traditional methods for measuring cable tensions.

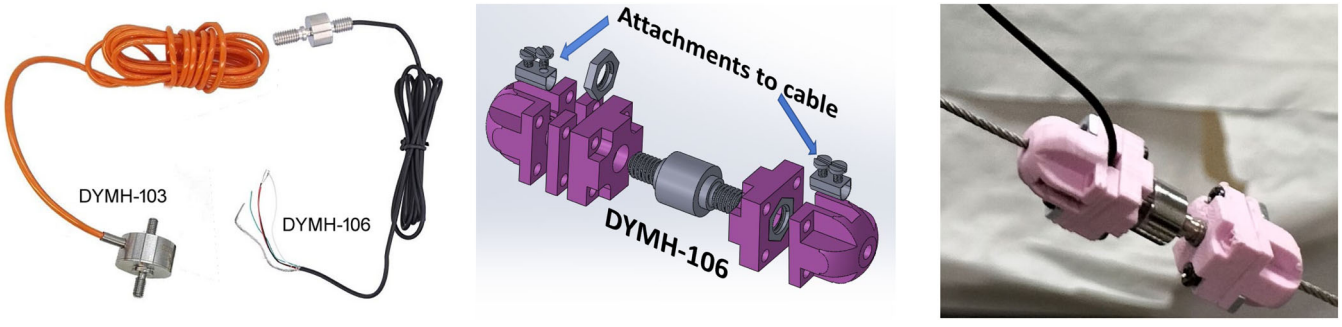

FIGURE 10 | Inline force sensor: left, commercial tension sensor DYMH, models 106 and 103; center, CAD representation of the enclosure; right, final appearance once attached to the cable.

TABLE 6 | Characteristics for the tension sensors DYMH 106 and 103.

	Sensitivity	Repeatability	Creep	Temperature sensitiveness
DYMH-106	2 (mv/V)	±0.5% F.S.	±0.1% F.S./30 min	±0.05% F.S./10°C
DYMH-103	1.5 (mv/V)	±0.03% F.S.	±0.2% F.S./30 min	±0.1% F.S./10°C

Abbreviation: F.S., full scale.

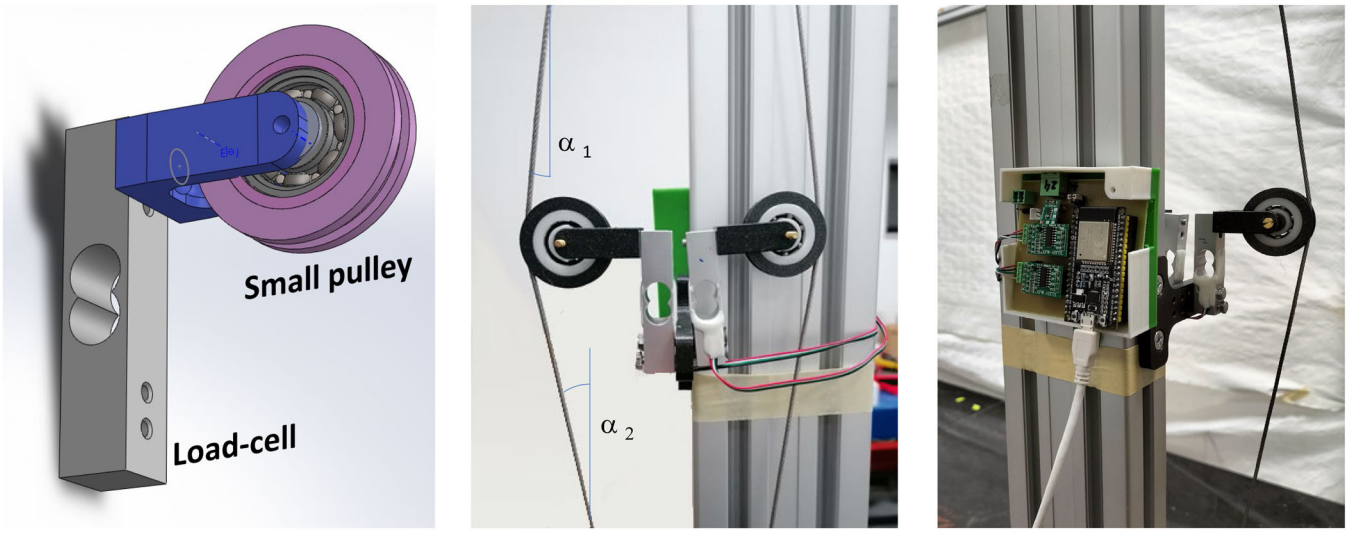

FIGURE 11 | CAD scheme and final setup of the loadcell-based sensor, with the small pulley pushing the load-cell.

As provided, the sensor cannot be directly attached to the cable. To this purpose, an enclosure with negligible weight plastic parts has been designed (see Figure 10). The source files for the CAD model have been uploaded in a repository and can be downloaded from (Gonzalez 2024). This figure also shows the sensor in series with the cable.

4.1.2 | Loadcell-Based Sensor

As illustrated in Figure 11, this second sensor employs a load cell, with one end actuated by a small pulley, altering the cable's trajectory as in the second and third schemes of Figure 9. However, the trajectory modification in the proposed scheme is much milder, barely causing any curvature in the cable. Additionally, compared to setup 2, it has the advantage that it does not need to be positioned near the drum but can be placed anywhere between the drum and the last directing pulley. Compared to setup 3, the scheme is much simpler, with only one pulley instead of three, and it does not force as many curvature changes in the cable. This same advantage is also present in comparison to the scheme proposed by Rubio-Gómez et al. (2021). The proposed sensor should be placed at a fixed intermediate position between the drum and a pulley or between two pulleys, ensuring that the exit angles of the cable exerting force on the sensor (α_1 and α_2 in central image of Figure 11) remain constant.

This sensor type measures tension indirectly, capturing the projection of the tension perpendicular to the cable's natural path.

$$F_{push} = T\sin(\alpha_1) + T\sin(\alpha_2). \tag{31}$$

The placement of the sensor sets the angles, affecting the ratio between the measured cable tension and the resulting force reading. Therefore, the sensor's position must remain fixed after calibration.

In fact, measuring these angles is unnecessary, as the calibration procedure establishes the relationship between cable tension and the sensor reading. The angles are only needed to choose the range of measurement, which for a maximum cable tension $\tau_{\max}$, yields a full-scale force equal to:

$$F_{F.S} = \frac{\tau_{\max}}{\sin(\alpha_1) + \sin(\alpha_2)}. \tag{32}$$

The CAD model source files are available at Gonzalez (2024).

4.2 | Connection to a Microcontroller

Both types of sensors measure traction forces (and compression forces, though irrelevant here) using a strain gauge. This gauge is a thin, long resistor fixed to a object that deforms under the applied force. As the object deforms, the resistor's resistance changes. Due to the small resistance change, an amplification circuit, with the HX711 being a popular choice and the one used in this work, is used to suppress the noise and amplify the signal. The connection schemes for both sensors are shown in Figure 12.

As shown in these figures, an additional microcontroller is required for the inline force sensor. This is because the sensor

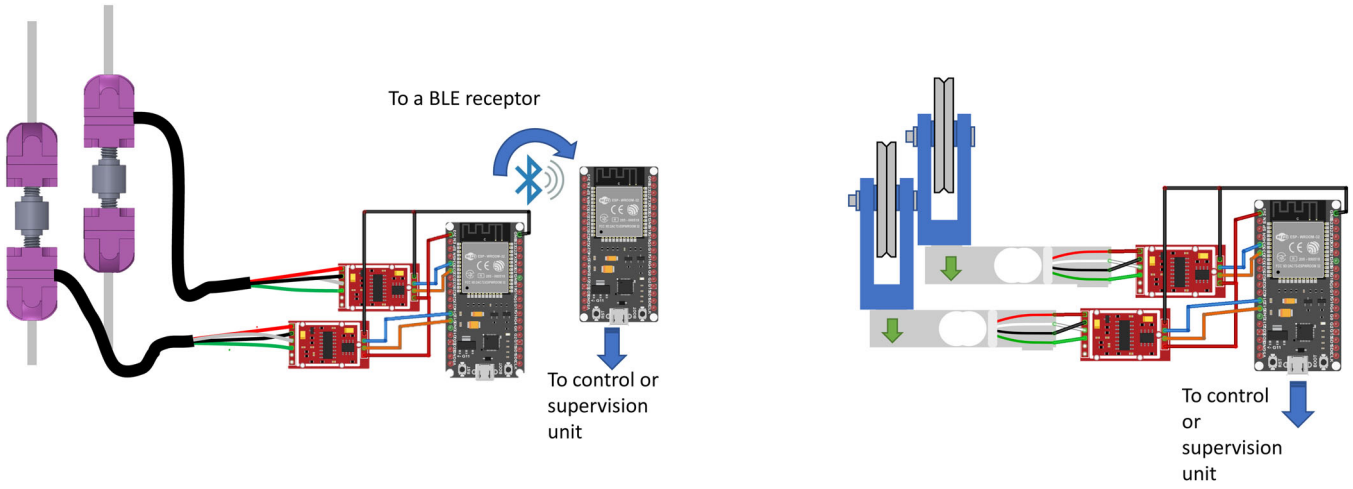

FIGURE 12 | Electrical connection of the inline force sensor (left) and the loadcell-based sensor (right) to a microcontroller ESP32.

must be positioned close to the moving EE, necessitating a wireless link to obtain the readings. In this work, Bluetooth Low Energy (BLE) notifications are sent from the server (at the EE) to the client (at the unit control). To offload the unit control from handling these periodic messages, a microcontroller is placed near the unit control to receive the BLE messages and forward them via a USB cable using a Virtual Com Port.

For the loadcell-based sensor, which is fixed to the robot frame, a wireless link is unnecessary. In this work, with distances between sensors and controller lower than 2 meters, a USB cable has been employed. For longer distances, a SPI link can be used.

4.3 | Calibration

Before using the tension sensors in the final robot, a calibration is needed to determine the relationship between the sensor reading and the applied tension. For this purpose, the setup shown in Figure 13 is arranged, in which known masses are hung at the end of the cable, and the corresponding tension measured. These masses cover a range from 0.10 to 6.70 kg.

In this configuration, to hang a test mass during calibration, it is necessary to use an additional pulley attached to the top of the frame, which makes the cable path configuration during calibration different from what will be in the final CDPM. This is not a concern for the inline force sensors, which are located at the end of the chain, close to the mass, and measure the tension of the cable provoked by the weights. In the case of the loadcell-based sensor, this additional pulley includes another source of static friction, that must be subtracted from the obtained reading if accurate measurements are required.

Figures 14 and 15 show the result of the calibration made to the four sensors: two inline force sensors and two loadcell-based sensors. For their calibration, seven probe masses have been hung, in ascending order. For each mass, five readings are taken after waiting for the measurement to stabilize, and their average value is recorded. Subsequently, the masses are measured again in descending order. It is evident that both types of sensors exhibit a fairly linear behavior, with no noticeable hysteresis. In all cases, the correlation factor exceeds 0.9994.

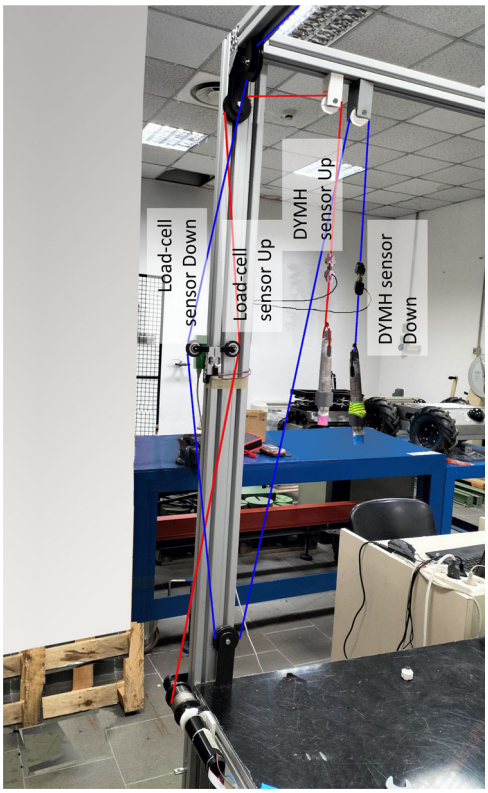

FIGURE 13 | Calibration setup for the inline force sensor and the loadcell-based sensor. The routing for the upper cable (the one attached to the upper DAP) is highlighted in red. The routing for the lower cable is highlighted in blue.

This allows obtaining, in a reasonably confident way, a relationship between the reading R and the cable tension T as

$$T(N) = \frac{R - t_0}{\alpha}, \tag{33}$$

where t_0 is the y-intercept, and α is a proportionality factor.

5 | Using the Sensors in a CDPM

Once the sensors have been calibrated, they are prepared to deliver cable tension measurements to the control or monitoring algorithm. Figure 16 presents the right hand part of the CDPM used for this experiment, in which one inline force sensor and the loadcell-based sensor are zoomed. For this last

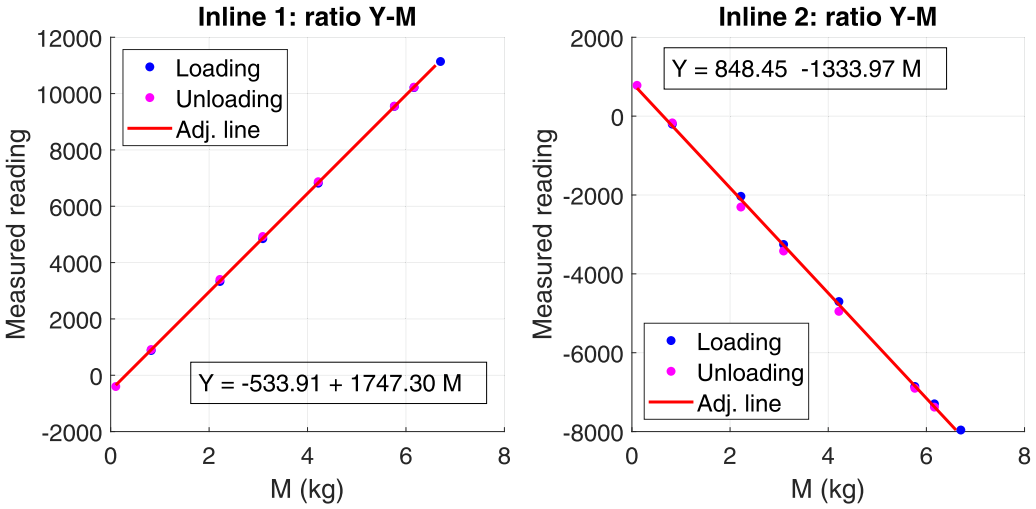

FIGURE 14 | Calibration for the inline force sensor.

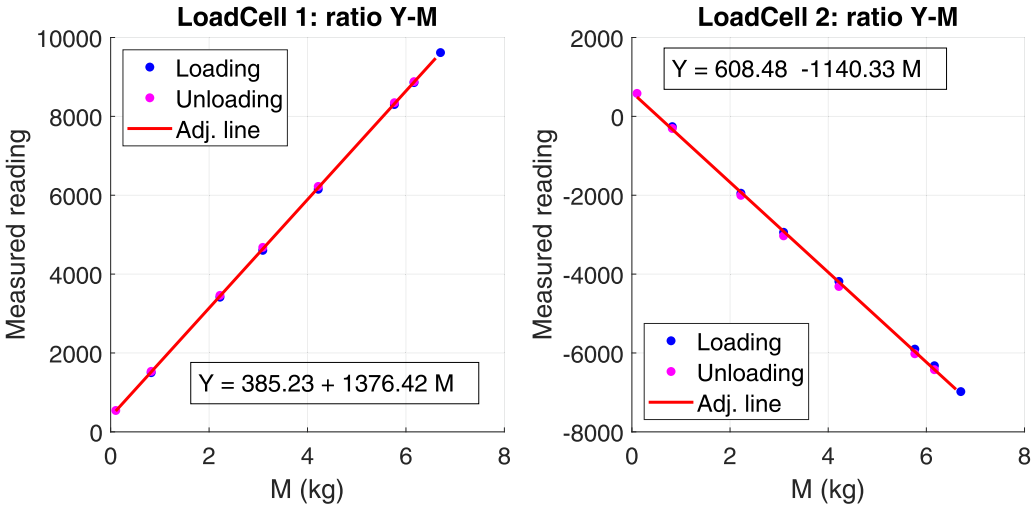

FIGURE 15 | Calibration for the loadcell-based sensor.

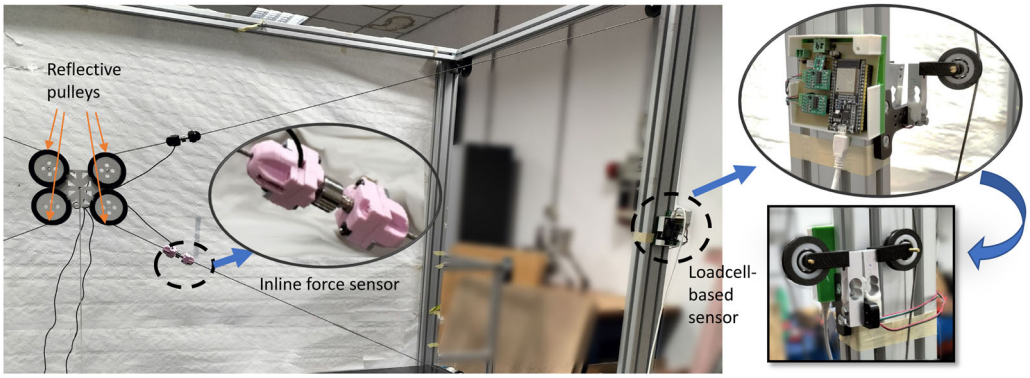

FIGURE 16 | CDPM used for the experiment, with details of one inline force sensor and one loadcell-based sensor.

one, the electronic card (with amplifier and microcontroller ESP32) is also shown that collects the measurements from two loadcell-based sensors. The reflective pulleys that improve the positioning accuracy are also illustrated. If sensors are not included but the motor current values are available (as with the ESCON 70/10), the following formula is traditionally used to estimate the cable tension τ under static conditions:

$$\tau\, r = k_{\phi}^{\tau}\, I\, r_{gb}, \tag{34}$$

where I_a is the armature current, r represents the pulley radius, k_{ϕ}^{τ} is the motor torque constant that relates the armature current to the internal torque, and r_{gb} is the gear ratio of the gearbox connected to the shaft rotor. It is worth noting that the variable used for feedback to the controller is the drum rotation angle (translated to the HSS), and that the actuation signal is the armature current of the DC motor. Therefore, the cable tension is only indirectly considered in the controller.

Even in static conditions, this equation needs information about the overall static friction from the motor to the end effector, which is often unavailable. Static friction is hard to model and causes noticeable hysteresis, degrading the performance of linear controllers, especially when motor direction is reversed. In dynamic conditions, the estimate worsens further due to additional torque from inertia and viscous friction.

The following experiment was conducted to demonstrate that the tension values estimated from (34) do not accurately reflect the actual cable ones. In this experiment, the end effector (EE) was positioned at five different locations (see Figure 17). Current values were increased to the motors from 0 to 1.7 A and then decreased back to 0 A, allowing time for the tension to stabilize after each change in current. Figure 18 shows the result of the experiment. The x-axis represents the tension value τ_{estim} in Newtons (N) estimated from (34), which is essentially the internal mechanical torque divided by the drum radius r and multiplied by r_{gb} to translate it to the LSS, that is

$$\tau_{estim} = \frac{k_{\phi}^{T} I_a r_{gb}}{r}. \tag{35}$$

The y-axis represents the measured tension values in Newtons (N) derived by using (33) with the stabilized readings.

Several conclusions can be drawn from analyzing these results:

- The measurements of the upper cable tension from the inline force sensor and the loadcell-based sensor match almost perfectly. For the lower cable, the match is reasonably good, though there are some outliers. The values from these sensors differ significantly from those estimated using (35), indicating that this formula is not a reliable method for estimating cable tension.
- The discrepancy is not just about scaling or shifting but also varies depending on whether the process involves loading or unloading. This disparity primarily arises from static friction, which exhibits strong hysteresis, combined with some other phenomena: the cable elasticity; the accommodation to a different tension distribution to fulfill the dynamics constrains given by (7); eccentricity in the coupling between the motor shaft and the drum; and non-uniform distribution of tension in the cable wound on the drum.

This disparity is likely to increase under dynamic conditions, highlighting the need for tension sensors if accurate cable tension measurements are required, rather than relying on the approximate estimates derived from the motor current.

6 | Discussion

This study presented two tension sensors for monitoring cable tension to avoid issues like sagging, slack, unrolling, or excessive tension that could increase power demand and potentially damage components. Both sensors demonstrated linear performance with minimal hysteresis during loading and unloading.

For the inline inline force sensor, the main drawbacks are their higher cost compared to load cells and the need for a wireless link to transmit the signal to the control unit. For non-dedicated communication links such as Bluetooth or WiFi, the link layout

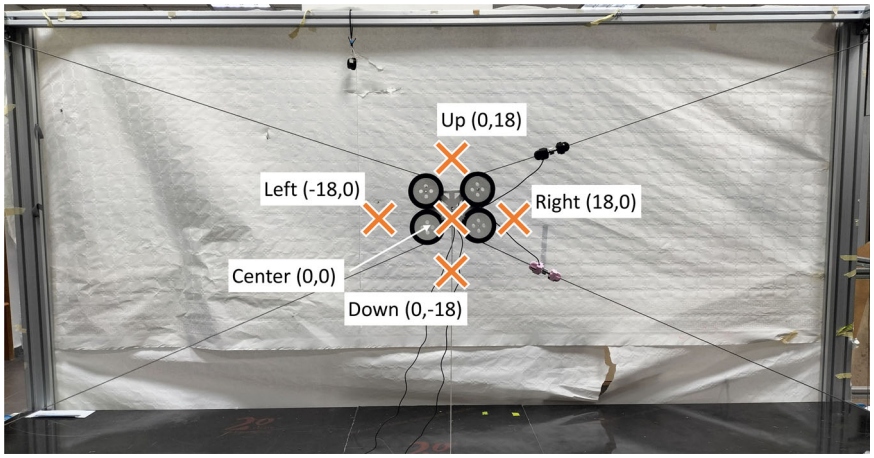

FIGURE 17 | Positions for the EE where the tension value estimated from the motor current is compared to the measured ones. The image shows the central position.

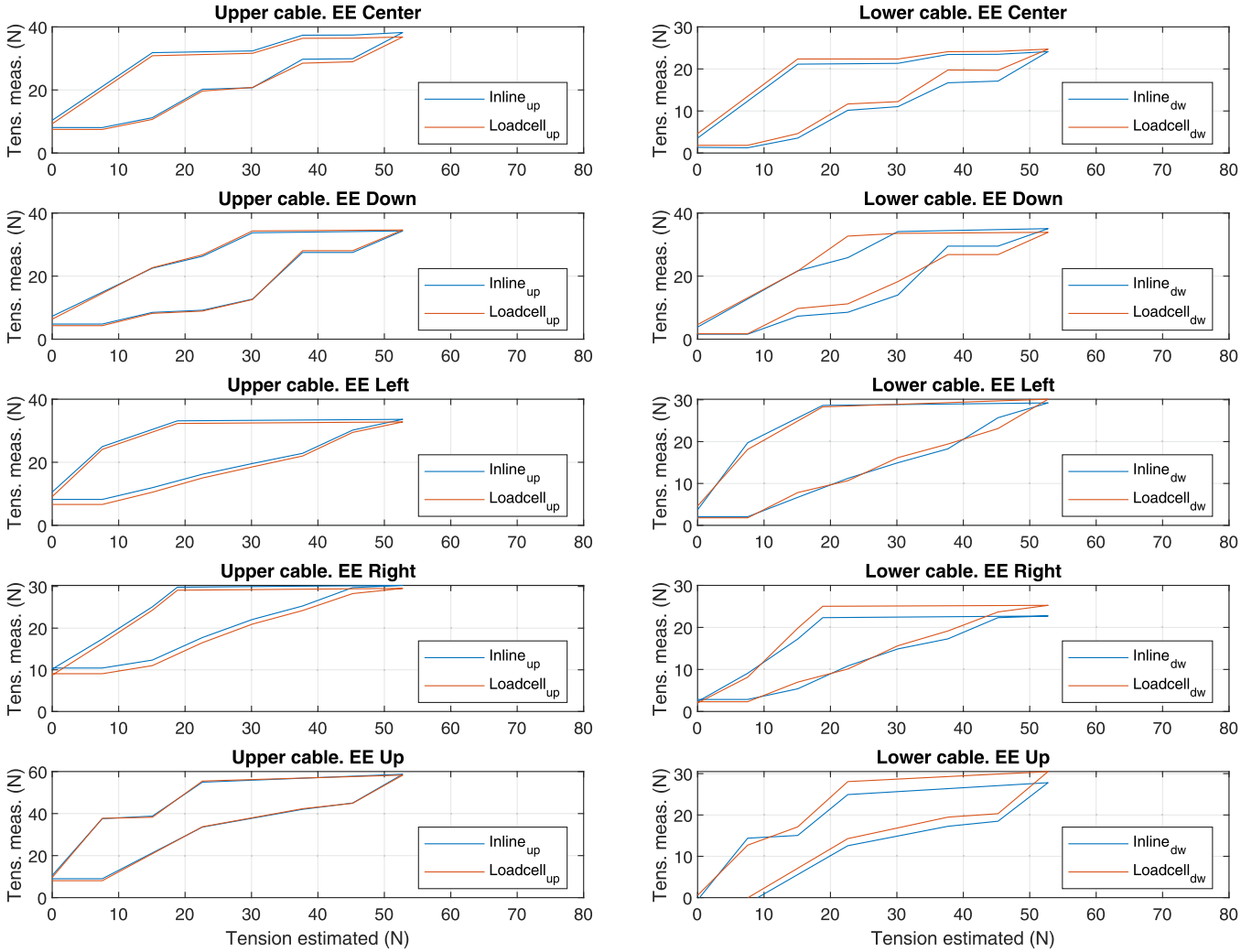

FIGURE 18 | Relationship between the tension value estimated from the motor current and the corresponding measured tension at various configurations.

requires a minimum time to establish the connection, that in the case of Bluetooth is not lower than 6 ms, even for the transmission of few bytes. During these experiments, only notification times equal or higher than 30 ms could be periodically maintained.

In the case of loadcell-based sensor, its calibration requires including an additional pulley, whose static friction gives rise to a slightly reduced value of the tension measured by the sensor. Additionally, the small pulley in the loadcell-based sensor introduces extra friction during the normal operation. As an advantage, the force measured by the load cell is the projection onto the perpendicular to the undisturbed direction of the cable. If, to minimally modify the cable path, small angles α_1 and α_2 are chosen, a load cell with a much smaller measuring range can be chosen.

Finally, an experiment was conducted to highlight the discrepancy between the measurements obtained from these tension sensors and the values estimated from the motor currents. This demonstrates that if accurate tension values are needed, estimates based on armature current are not reliable.

Both sensors exhibit optimal performance under static conditions. However, the HX711 amplifier proves to be too slow, with conversion rates around 100 ms. As a future improvement, the replacement of this amplifier with a faster one is planned. Additionally, it is intended to replace the Bluetooth link of the inline force sensor with a tailored communication protocol using a generic radio frequency link.

Acknowledgments

This research was supported by the University of Jaen.

Data Availability Statement

The data that support the findings of this study are openly available in Mendeley Data at https://data.mendeley.com/datasets/493rdzy3mm/1, reference number https://doi.org/10.17632/493rdzy3mm.1.

References

Albus, J., R. Bostelman, and N. Dagalakis. 1992. "The NIST Robocrane." *Journal of Robotic Systems* 97, no. 3: 373–385. https://tsapps.nist.gov/publication/get_pdf.cfm?pub_id=820409.

Barbazza, L., F. Oscari, S. Minto, and G. Rosati. 2017. "Trajectory Planning of a Suspended Cable Driven Parallel Robot With Reconfigurable End Effector." *Robotics and Computer-Integrated Manufacturing* 48: 1–11. https://doi.org/10.1016/j.rcim.2017.02.001.

Bosscher, P., A. Riechel, and I. Ebert-Uphoff. 2006. "Wrench-Feasible Workspace Generation for Cable-Driven Robots." *IEEE Transactions on Robotics* 22, no. 5: 890–902. https://doi.org/10.1109/TRO.2006.878967.

Bosscher, P., R. L. Williams, L. S. Bryson, and D. Castro-Lacouture. 2007. "Cable-Suspended Robotic Contour Crafting System." *Automation in Construction* 17, no. 1: 45–55. https://doi.org/10.1016/j.autcon.2007.02.011.

Brown, G. 1985. "Skycam: An Aerial Robotic Camera System." *BYTE*, 122. https://archive.org/details/byte-magazine-1985-10/page/n121/mode/2up.

Bruckmann, T., L. Mikelsons, T. Brandt, M. Hiller, and D. Schramm. 2008. "Wire Robots Part I Kinematics, Analysis & Design." In *Parallel Manipulators, New Developments*, edited by J.-H. Ryu, 109–130. Rijeka: IntechOpen. https://doi.org/10.5772/5365.

CarpioAlemán, M. A., R. Saltaren, A. Rodriguez, G. Portilla, and J. D. Placencia. 2019. "Rotational Workspace Expansion of a Planar Cdpr With a Circular End-Effector Mechanism Allowing Passive Reconfiguration." *Robotics* 8, no. 3: 57. https://doi.org/10.3390/robotics8030057.

Chen, G., H. Muriki, A. Sharkey, C. Pradalier, Y. Chen, and F. Dellaert. 2023. "A Hybrid Cable-Driven Robot for Non-destructive Leafy Plant Monitoring and Mass Estimation Using Structure From Motion." In *2023 IEEE International Conference on Robotics and Automation (ICRA)*, edited by IEEE Robotics and Automation Society, 11809–11816. London: IEEE. https://doi.org/10.1109/ICRA48891.2023.10161045.

Feyrer, K. 2007. *Wire Ropes. Tension, Endurance, Reliability*. Berlin: Springer-Verlag.

Gonzalez, A. 2024. Tension Sensors. Mendeley Data. Amsterdam: Elsevier. https://doi.org/10.17632/493rdzy3mm.1.

Gonzalez-Rodriguez, A., F. Castillo-Garcia, E. Ottaviano, P. Rea, and A. Gonzalez-Rodriguez. 2017. "On the Effects of the Design of Cable-Driven Robots on Kinematics and Dynamics Models Accuracy." *Mechatronics* 43: 18–27. https://doi.org/10.1016/j.mechatronics.2017.02.002.

Idà, E., D. Marian, and M. Carricato. 2020. "A Deployable Cable-Driven Parallel Robot With Large Rotational Capabilities for Laser-Scanning Applications." *IEEE Robotics and Automation Letters* 5, no. 3: 4140–4147. https://doi.org/10.1109/LRA.2020.2989669.

Iturralde, K., and T. Bock. 2018. "Integrated, Automated and Robotic Process for Building Upgrading With Prefabricated Modules." *35th ISARC* 1: 340–347. https://doi.org/10.22260/ISARC2018/0048.

Izard, J.-B., A. Dubor, P.-E. Hervé, et al. 2017. "Large-Scale 3D Printing With Cable-Driven Parallel Robots." *Construction Robotics* 1, no. 1: 69–76. https://doi.org/10.1007/s41693-017-0008-0.

Juárez-Pérez, S., A. González-Rodriguez, D. R.-R. GuillermoRubio-Gómez, E. Ottaviano, and F. J. Castillo-Garcia. 2021. "Closed Loop Cable Robot for Large Horizontal Workspaces." *Smart Structures and Systems* 27, no. 2: 397–406. https://doi.org/10.12989/sss.2021.27.2.397.

Kraus, W., M. Kessler, and A. Pott. 2015. "Pulley Friction Compensation for Winch-Integrated Cable Force Measurement and Verification on a Cable-Driven Parallel Robot." *Proceedings of International Conference on Robotics and Automation* 2015, no. June: 1627–1632. https://doi.org/10.1109/ICRA.2015.7139406.

Merlet, J.-P. 2000. *Parallel Robots*. Dordrecht: Springer. https://doi.org/10.1007/978-94-010-9587-7.

Merlet, J.-P. 2008. "Kinematics of the Wire-Driven Parallel Robot MARIONET Using Linear Actuators." In *2008 IEEE International Conference on Robotics and Automation*, edited by S. Hutchinson, 3857–3862. Pasadena, California: IEEE. https://doi.org/10.1109/ROBOT.2008.4543803.

Ogata, K. 2010. *Modern Control Engineering*, 5th ed. México: Pearson.

Ottaviano, E., M. Ceccarelli, and F. Palmucci. 2009. "An Application of Catrasys, a Cable-Based Parallel Measuring System for an Experimental Characterization of Human Walking." *Robotica* 28: 119–133. https://doi.org/10.1017/S0263574709990417.

Piao, J., E. S. Kim, H. Choi, et al. 2019. "Indirect Force Control of a Cable-Driven Parallel Robot: Tension Estimation Using Artificial Neural Network Trained by Force Sensor Measurements." *Sensors (Switzerland)* 19, no. 11: 2520. https://doi.org/10.3390/s19112520.

Pott, A., T. Bruckmann, and L. Mikelsons. 2009. "Closed-form force distribution for parallel wire robots." In *Closed-form Force Distribution for Parallel Wire Robots*, edited by A. Kecskeméthy and A. Müller, 25–34. Berlin: Springer. https://doi.org/10.1007/978-3-642-01947-0_4.

Pott, A., C. Meyer, and A. Verl. 2010. "Large-Scale Assembly of Solar Power Plants With Parallel Cable Robots." In *ISR 2010 (41st International Symposium on Robotics) and ROBOTIK 2010 (6th German Conference on Robotics)*, edited by IEEE, 1–6. Munich: VDE Verlag. https://ieeexplore.ieee.org/abstract/document/5756909.

Roberts, R. G., T. Graham, and T. Lippitt. 1998. "On the Inverse Kinematics, Statics, and Fault Tolerance of Cable-Suspended Robots." *Journal of Robotic Systems* 15: 581–597. https://doi.org/10.1002/(SICI)1097-4563(199810)15:10<581::AID-ROB4>3.0.CO;2-P.

Rubio-Gómez, G., S. Juárez-Pérez, A. Gonzalez-Rodríguez, et al. 2021. "New Sensor Device to Accurately Measure Cable Tension in Cable-Driven Parallel Robots." *Sensors* 21, no. 11: 3604. https://doi.org/10.3390/s21113604.

Schröder, S. 2021. "Under Constrained Cable-driven Parallel Robot for Vertical Green Maintenance." In *Cable-Driven Parallel Robots*, edited by M. Gouttefarde, T. Bruckmann, and A. Pott, 389–400. Cham: Springer International Publishing. https://link.springer.com/content/pdf/10.1007/978-3-030-75789-2_31.pdf.

Thanh, T., and N. Truong Thinh. 2022. "Winch-Integrated Cable Force Measurement and Verification on Driven Cable Parallel Robot 6 d.o.f." *International Journal of Mechanical Engineering and Robotics Research* 11, no. 10: 755–760. https://doi.org/10.18178/ijmerr.11.10.755-760.

Yang, N., J. Li, M. Xu, and S. Wang. 2022. "Real-Time Identification of Time-Varying Cable Force Using an Improved Adaptive Extended Kalman Filter." *Sensors* 22, no. 11: 4212. https://doi.org/10.3390/s22114212.

Appendix A

Evaluation of Friction Parameters

The static friction value, τ_{fr}^{st}, which combines the rotor, gearbox, and screw, was obtained by progressively increasing a suspended weight retained by the actuator, until the weight value that overtakes static friction is reached and it begins to descend. The resulting mass ($M = 0.62$ kg) is then multiplied by g and the pulley radius, r_{drum}, to obtain τ_{fr}^{st}. The value for the rotor alone cannot be experimentally deduced since its shaft is attached to the gearbox without possibility of analyzing separately.

With regard to the value of the dynamic friction, $B_{gb+drum}$, it has been obtained by subtracting B_{rotor}^{HSS} (see Table 1) from the value of the total dynamic friction B_t. In turn, this value is obtained by dropping a mass attached to the actuator and counting the time t_f needed to complete the falling trajectory. The following equation, that provides the linear displacement h for a falling mass, has been used:

$$h = \frac{P_{red}}{B_t} t_f + \frac{P_{red} M}{B_t^2} \left(exp\left(-\frac{B_t}{M} t_f \right) - 1 \right) \tag{A1}$$

being

$$P_{red} = M \cdot g - \frac{\tau_{fr}^{st}}{r_{drum}} \tag{A2}$$

with B_t the unknown overall friction coefficient for the linear movement, t_f the time to fall, and M the mass of the falling object. The previous equation has been obtained by doubly integrating

$$\begin{gathered} M\ddot{d} + \frac{J_t}{r_{drum}}\ddot{d} + B_t\dot{d} = P_{red} \quad \text{with } \dot{d}(0) = d(0) = 0 \\ d(t_f) = h, \end{gathered} \tag{A3}$$

where J_t (the sum of all inertia values) can be disregarded for large t_f in a first approximation. After obtaining the overall linear friction coefficient, τ_{fr}^{st} is obtained as:

$$\tau_{fr}^{st} = B_t r_{drum}^2 - B_{rotor}^{HSS} r_{gb}^2. \tag{A4}$$

Appendix B

Evaluation of the Coefficients of Elasticity

Among the most commonly used materials in CDPM cables is stainless steel, although it is also common to find synthetic fibers such as Kevlar, UHMWPE (Dyneema), and Vectran. When using steel, the cables are arranged as ropes composed of strands spirally wound to increase the cable's flexibility and stress distribution, which is necessary for winding on the drum or changing direction on the pulleys. This arrangement reduces the overall elastic modulus of the assembly. Feyrer (2007) provides an expression to estimate this value, although the author notes that the actual value will be lower than the estimated value the smaller the stress level and the higher the number of strands in the rope. Additionally, a residual strain (around 0.5%) must be taken into account, which appears after a few load and unload cycles.

Starting from stress-strain test conducted for the cable used in the presented setup, a value of 48.9 GPa Gonzalez (2024) is obtained, significantly lower than the values found in Feyrer (2007), around 90–110 $\mathrm{kN/mm^2}$, for thicker ropes.

For a calculated cross section of 1.89 $\mathrm{mm^2}$, and a cable length of 6 m the following coefficients of elasticity are obtained:

$$K_A = K_B = 7560\,\mathrm{N/m}. \tag{B1}$$